Sensors and Actuators A 312 (2020) 112100

Contents lists available at ScienceDirect

Sensors and Actuators A: Physical

journal homepage: www.elsevier.com/locate/sna

Proof of concept of a novel absolute rotary encoder☆

Lorenzo Iafolla[a,*], Massimiliano Filipozzi[a], Sara Freund[a], Azhar Zam[b], Georg Rauter[c], Philippe Claude Cattin[a]

[a] Center for medical Image Analysis & Navigation (CIAN), Department of Biomedical Engineering, University of Basel, Gewerbestrasse 14, 4123, Allschwil, Switzerland
[b] Biomedical Laser and Optics Group (BLOG), Department of Biomedical Engineering, University of Basel, Gewerbestrasse 14, 4123, Allschwil, Switzerland
[c] Bio-Inspired RObots for MEDicine-Lab (BIROMED), Department of Biomedical Engineering, University of Basel, Gewerbestrasse 14, 4123, Allschwil, Switzerland

ARTICLE INFO

Article history:
Received 12 December 2019
Received in revised form 12 April 2020
Accepted 22 May 2020
Available online 30 May 2020

Keywords:
ASTRAS
Angular sensor
Absolute rotary encoder
Miniaturized rotary encoder
Medical tracking device

ABSTRACT

Rotary encoders are used in many applications that require monitoring or controlling mechanical systems such as robots. Typically, small rotary encoders have poor resolution; this is unfortunate for applications such as robotics in medical surgery procedures. For example, in an articulated robotic endoscope, miniaturization is mandatory and, when automation is desired, high accuracy to track the shape and pose of the device is required; small (few millimeters) and accurate (few hundred arcsec) rotary encoders are thus needed.

Previously, we introduced a novel concept of a miniaturizable angular sensor, called ASTRAS (Angular Sensor for TRAcking System). This was presented as a basic element of a tracking system for articulated endoscopes. The principle of measurement of ASTRAS is based on processing a shadow image cast by a shadow mask onto an image sensor. The characterization of the first prototype of ASTRAS was very promising, however, its angular range of about ±30 degrees was too limiting for many practical applications.

In this work, we present an extension of the concept mentioned above to a rotary encoder that can measure one full rotation of 360 degrees thus the name is ASTRAS360. Its working principle bases on encoding the shadow image using colored light to distinguish different angular sectors. The identification of the sector corresponds to a coarse angular measurement, which is afterward refined using the same technique as in ASTRAS. We implemented this concept, realizing a prototype and an algorithm to calculate the angle from the shadow image. The experiments demonstrated the validity of this concept and showed encouraging results with a precision of ∼0.6 arcsec and 6σ-resolution of 3.6 arcsec corresponding to 19 bits.

1. Introduction

Rotary encoders are used widely in mechanical systems that require monitoring and/or controlling of a moving part. In some fields, such as in medical robotics [1,2], the requirements on size, accuracy, and reliability (i.e. absolute measurement) are very demanding, and off-the-shelf rotary encoders are not always able to address them. For this reason, our objective is to develop an absolute rotary encoder able to outperform the existing ones in terms of resolution and size. Therefore, this work aims to extend the measurement range of a novel concept of a miniaturizable, absolute, high accuracy, angular sensor called ASTRAS (Angular Sensor for TRAcking Systems).

The concept of ASTRAS is described in [3] and it belongs to a group of sensors called "shadow sensors". They measure the position of a light source, or the direction of the impinging light, by detecting a shadow image [4–10]. As described in [3], ASTRAS measures the angle between a stator and a rotor. Its components are arranged in such a way that each value of the input angle β, corresponds to a specific shadow image. The validity of the ASTRAS concept was demonstrated, and its performances characterized, resulting in a sensor with absolute encoding, precision of ∼0.6 arcsec, 6σ-resolution of ∼3.6 arcsec, linearity error

☆ This work was part of the MIRACLE project funded by the Werner Siemens-Foundation (Zug, Switzerland).

* Corresponding author at: Department of Biomedical Engineering, University of Basel, Gewerbestrasse 14, 4123, Allschwil, Switzerland.
E-mail addresses: lorenzo.iafolla@unibas.ch, lorenzo.iafolla@outlook.it (L. Iafolla).

https://doi.org/10.1016/j.sna.2020.112100

of ∼21 arcsec (rms) over a range of 17 degrees, thermal stability of ∼4 arcsec/°C, and long term drift of ∼2 arcsec/day. The miniaturization potential of ASTRAS was discussed in [11], and the possibility of acquiring and processing the data in real-time was investigated in [12]. Even though these results were promising, the angular range of ASTRAS was rather small, ±30 degrees thus limiting its applicability. Therefore, this work focuses on the method and the characterization of a concept, called ASTRAS360, to measure absolute angles over one full rotation.

As ASTRAS360 represents a new concept of a rotary encoder (RE), it also has to be compared to other RE concepts. Among the most used RE, there are potentiometers, magnetic encoders, synchros, resolvers, optical encoders and inductosyns [13–18]. Here, we focus only on magnetic encoders, optical encoders and inductosyns as they belong to the same class of accuracy (better than 1 arcmin) that we are targeting for ASTRAS360.

Magnetic encoders detect the rotation of a magnet attached to the rotor. Often the sensing part, attached to the stator, is a Hall Effect device in chip form whose output voltage depends linearly from the rotation angle of the rotor. Though these sensors are quite tolerant to foreign matter, they are typically not chosen for applications in harsh environments or shock conditions [17]. The main advantages of the magnetic sensors are absolute encoding, good robustness, and their tolerance to liquids. However, they have a modest performance because it is limited by interferences with magnetic material or with electrical cables in proximity, hysteresis effects, and temperature variations. An example of a small, off-the-shelf, absolute, magnetic, rotary encoder is the AS5047U by AMS [19]. It has a chip size $5 \times 6.4\,mm^2$ (no data related to the rotor are reported) and features a linearity-error down to ∼2900 arcsec and resolution down to 79 arcsec (14 bits).

The optical encoders have an optical sensor head, which acts as the stator, and a grated optical disk or ring which is the rotor. The light, emitted by a source, passes through or is reflected by the grating and is then detected by the sensing head. The signal generated is a sine or square wave whose phase is related to the rotation of the disk. Their main advantages are the high resolution and accuracy (down to 0.01 arcsec) [20–24], and it is a well-known and developed technology. Typically, these are relative encoders, but absolute encoding is possible at the cost of increased hardware complexity by using several gratings with different pitches or more sophisticated solutions such as a single-track periodic Gray code [25]. However, they suffer from multiple limitations related to the alignment (and the displacement) of their sensing head with the grating, and of the rotation axis with the axis of the disk (eccentricity) [26]. Several examples of off-the-shelf optical rotary encoders are available on the market. The MAS10 by CUI Inc. [27], for instance, is a small absolute encoder featuring a diameter of 13 mm and a height of 15.5 mm but quite poor resolution (∼5062 arcsec corresponding to 8 bits). Another prototype of the same class of encoders with a size of $10 \times 10 \times 10\,mm^3$ and a resolution of ∼1266 arcsec (10 bits) has been described in [28]. Finally, the PA2-50 by Faulhaber [29], has been reported to be as small as 6 mm in diameter but this comes at the cost of being a relative encoder and featuring a reduced resolution of 7 degrees).

Inductosyn [30] (and its equivalent Incoder [31]) is a technology that provides very high performance. The measurement of the angular position of the rotor bases on the electrical coupling between windings produced by printed-circuit techniques. One winding is printed on the stator and it is excited with alternating current; this induces an output current in the windings printed on the rotor. The main advantages of the inductosyn are its high accuracy, the possibility for absolute encoding, reliability, and robustness. However, encoders of this type are typically quite expensive, and for very high accuracy measurements (down to 1 arcsec), they require a fine alignment to reduce eccentricity. The smallest off-the-shelf absolute Incoders have a diameter of roughly 40 mm and a height of 11.2 mm with a resolution of 9.89 arcsec (17 bits) and a systematic error of ∼350 arcsec.

The proposed ASTRAS360 sensor has its pros and cons, but a comparison between the various technologies can only be done in the framework of a specific application. As discussed in [3], an essential property of ASTRAS360 is the possibility of extending the same concepts and methods to two degrees of freedom (DOF) using one single sensor, i.e., to measure rotations about two orthogonal axes simultaneously. This is important, for example, for sensing the shape of a continuum robot that is composed of a sequence of rigid links [32,33]. In this case, one ASTRAS360 sensor can measure the two tilt angles between two contiguous links.

Furthermore, ASTRAS360 seems to be very promising in terms of resolution. This usually depends on the size of the rotary encoder and is thus an application-specific tradeoff. For applications such as minimally invasive surgical robotics, we believe that the proposed concept has the potential to outperform the other technologies. Indeed, even using a miniaturized image sensor, such as the NanEye by AMS [34], volume $1 \times 1 \times 0.5\,mm^3$ and pixel size $3 \times 3\,\mu m^2$, we could build a prototype of ASTRAS with a systematic error of 32 arcsec RMS and precision (standard deviation of repeated measurement) down to 5 arcsec [11]. This precision coincides to a 6σ-resolution (that is defined as six times the precision [35],) equal to $6 \times 5 = 30$ arcsec and corresponding to ∼16 bits. Although this was not yet an utterly miniaturized version of ASTRAS (other components, such as the rotary mount, were still big), we expect to achieve the same performance with a miniature version. Only the Incoder performs better in terms of resolution. Still, we believe that using the NanEye image sensor and a small ball bearing (diameters down to 1.6 mm are available in [36]), ASTRAS360 can be scaled down to a final diameter of 10 mm or even smaller. On the other side, using a slightly larger ($5.7 \times 4.28\,mm^2$) image sensor but with smaller pixel size ($2.2 \times 2.2\,\mu m^2$), such as the Ximea MU9PC used in [3], we could achieve a 6σ-resolution down to 3.6 arcsec. We believe that, in terms of resolution, the intrinsic advantage of ASTRAS360 relies on the small size of the pixels of the image sensor that enables measuring tiny differences between the shadow images.

However, before tackling the challenge of miniaturization or that of measuring over two DOFs, a good understanding of the concept and of the required image processing steps for ASTRAS360 is key. Focusing on this goal, we implemented the first prototype of ASTRAS360 and evaluated experimentally its working principle.

The working principle and a simplified model of ASTRAS360 are discussed in Section 2. As it is a crucial part for the proper functioning of the sensor. Section 3 described to the required image processing algorithms. To characterize the properties of ASTRAS360, we developed a prototype described in Section 4. Finally, the results of the experiments are discussed in Section 5, providing a validation of the working principle and an estimation of the performance.

2. Working principle and simplified model

Fig. 1 shows a conceptual cross-sectional drawing of ASTRAS360. The mechanical constraint, represented by the red arrows, limits the degrees of freedom in a way that only the rotation defined by the angle β is possible. The stator, which is the static part of the system, includes the image sensor, the shadow mask, and the LED. The rotor, which is the moving part of the system, has several (e.g. 8) mirrors with colored surfaces. As shown in Fig. 1, the light emitted by the LED is reflected by one of the mirrors attached to the rotor (mirror H for that specific value of β). The reflected light, or in an equivalent formulation, the

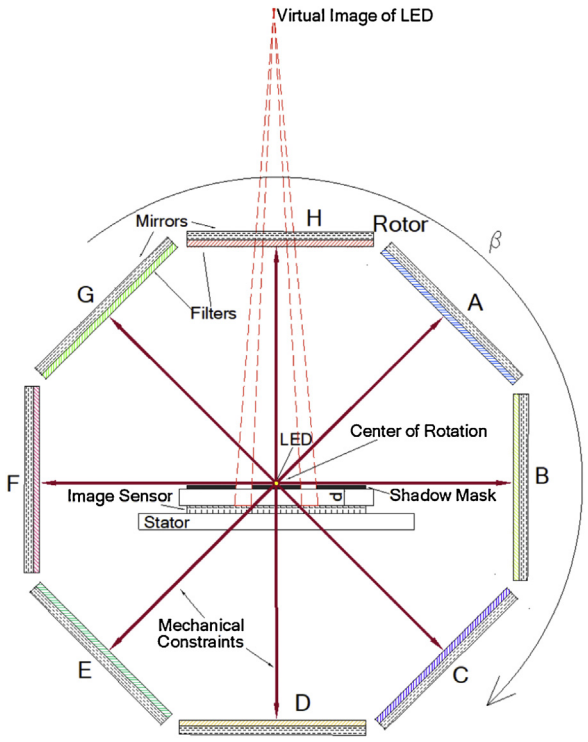

Fig. 1. ASTRAS360 conceptual drawing. (For interpretation of the references to color in the text, the reader is referred to the web version of this article).

light emitted by the virtual image of the LED, then casts a shadow onto the image sensor due to the shadow mask. The position, the shape, and the color of the shadow depends on β (see Video 1 and 2), that can be therefore evaluated. To define the variables of the system and illustrate the geometric relations, we use Fig. 2, which shows a more detailed view of Fig. 1, with only two mirrors shown. However, it is easy to generalize the definitions for more mirrors.

For each mirror, we can define one interval of β, i.e. Γ_A and Γ_B in Fig. 2, and a reference value, i.e. β_{AA} and β_{BB}. The intervals Γ_A and Γ_B are defined as all the values of β in which the corresponding mirror contributes to the shadow image i.e., light is reflected by this mirror and reaches the image sensor. In this simplified model, β_{AA} and β_{BB} are defined in a way that the corresponding mirrors A and B are parallel to the image sensor (for example, when β=β_{AA}, the mirror A is parallel to the image sensor). We also define the reference shadow images (or just reference images) R_{AA} and R_{BB} obtained when β=β_{AA} and β=β_{BB}. Finally, the "shadow A" is the contribution of the mirror A to the shadow image and similarly for the "shadow B" (see the reference shadow images R_{AA} and R_{BB} in Fig. 3, which are consistent with Fig. 2).

Considering only one mirror at a time, it is easy to see that, when $\beta \in \Gamma_A$, an input shadow image can be obtained by shifting the reference image R_{AA}. According to [3], the following input-output relation for mirror A ($\beta \in \Gamma_A$) can be used for all mirrors:

$$shift_A = d \cdot tan\left(\beta - \beta_{AA}\right) \approx d \cdot \left(\beta - \beta_{AA}\right) \tag{1}$$

Where $shift_A$ is the translation distance of the shadow A with respect to its reference position in R_{AA}; d is the distance between the shadow mask and the image sensor and it determines, by definition, the sensitivity. As is evident from Eq. (1), ASTRAS360 is a non-linear sensor, but, for small values of β-β_{AA}|, a linear approximation is possible. According to Eq. (1), we can calculate β as follow:

$$\beta = arctan\left(\frac{shift_A}{d}\right) + \beta_{AA} \approx \frac{shift_A}{d} + \beta_{AA} \tag{2}$$

Using a single mirror, the range of measurement $[\beta^-;\beta^+]$ is theoretically limited between $[-90;+90]$ degrees, as outside of this range, the light would no longer be cast onto the image sensor; in a practical case like the one described in [3], the range was even smaller ($[-30;+30]$ degrees). As demonstrated in [3], the range $[\beta^-;\beta^+]$ for ASTRAS360 is given by:

$$\beta_{AA}^{\pm} = arctan\left(\frac{\pm L_{AA}}{d}\right) + \beta_{AA} \approx \pm\frac{L_{AA}}{d} + \beta_{AA} \tag{3}$$

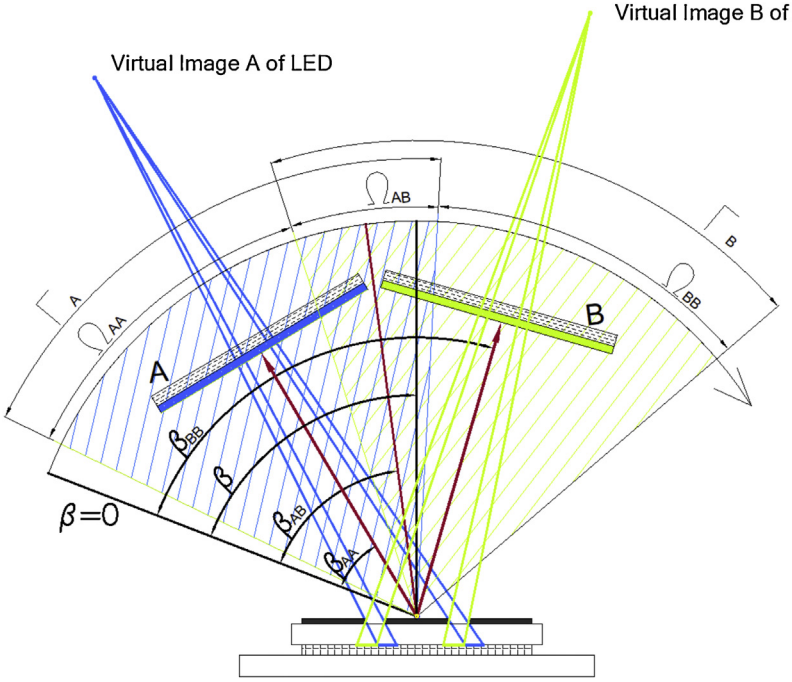

Fig. 2. Simplified version of ASTRAS360 featuring only two mirrors. In this state of ASTRAS360, the image sensor would capture a shadow image like R_{AB} in Fig. 3. (For interpretation of the references to color in the text, the reader is referred to the web version of this article).

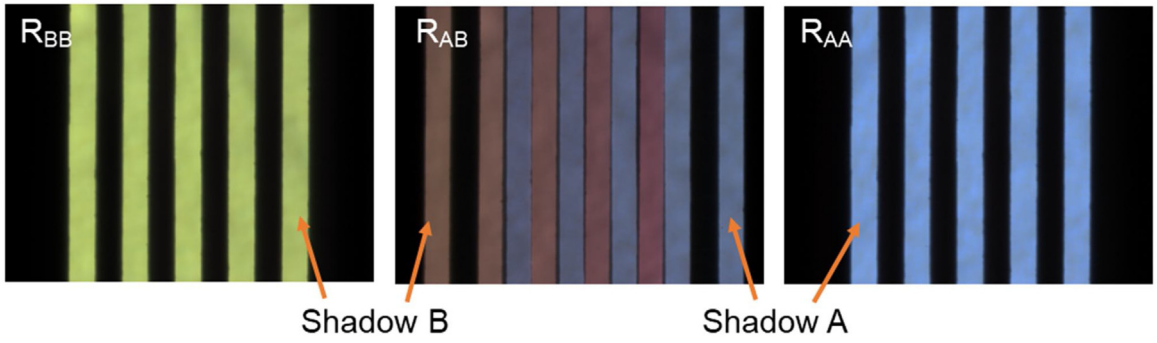

Fig. 3. Reference shadow images R_{AA}, R_{AB}, and R_{BB} of sectors Ω_{AA}, Ω_{AB}, and Ω_{BB} (the order of the images is consistent with Fig. 2). Shadow B was generated by mirror B whose color filter was pale green. This appeared in both the shadow images R_{BB} and R_{AB}. Similarly, shadow A was generated by mirror A whose color filter was neon blue. It appeared in shadow image R_{AA} and R_{AB}. A drift of the hue in the two-shadow image R_{AB} is visible. In fact, the hue of shadow B drifts from pale green in R_{BB} towards the brown in R_{AB}. (For interpretation of the references to color in this figure legend, the reader is referred to the web version of this article).

where $\pm L_{AA}$ is the range of $shift_A$ that still allows measuring with shadow A. Eventually, the usable range $\left[\beta_{AA}^{-}; \beta_{AA}^{+}\right]$ also depends on the image processing algorithm and we can only asses that $[\beta_{AA}^{-}; \beta_{AA}^{+}] \subseteq \Gamma_A$. Yet, if the system is designed such that the range of measurement of each mirror always overlaps with that of the contiguous mirrors, then the measurement is always possible. Consequently, as the name suggests, the range of measurement of ASTRAS360 is 360 degrees.

However, before measuring β, the interval Γ has to be identified to assign a reference value to β in Eq. (2) (e.g. the reference is β_{AA} when the interval is Γ_A). This can be done because the angular intervals are encoded by the different colors of the mirror filters. In particular, each mirror has a specific signature corresponding to a particular hue of the light (i.e., a particular distribution of values of the hue). In other words, identifying Γ_A by measuring the hue, provides β_{AA}, which already yields a coarse estimation of β; then, this estimation is refined by measuring the $shift_A$ using Eq. (2). This new method to measure a rotational angle presents several challenges described in the following.

First of all, some transition values of β are in the angular intervals Γ of more contiguous mirrors. For example, in Fig. 2 the interval Ω_{AB} identifies the overlap between Γ_A and Γ_B where both mirrors, A and B, contribute to the shadow. These transition angles generate shadow images consisting of the overlap of the light from both mirrors. For example, the shadow image R_{AB} in Fig. 3 is the overlap of the shadow A generated by the mirror A and the shadow B from mirror B. We will refer to these images as "two-shadow images" to differentiate them from the "single-shadow images" (e.g. R_{AA} and R_{BB} in Fig. 3) that are recorded when only one mirror contributes to the appearance of a shadow image. Correspondingly, we define the related intervals Ω of β as "two-shadow sectors" and "single-shadow sectors".

As a consequence of the full 360 ° range of ASTRAS360, the two-shadow sectors are unavoidable (this is also visible from Video 1). In principle, also three shadows images are possible but can be avoided using some technical solutions, as explained in Section 4. Consequently, we can split the full range of measurement in single-shadow sectors and two-shadow sectors for a total number of 16 sectors (two per mirror). We associate each sector to a double index identifying the mirror (or mirrors); for example in Fig. 2, the single-shadow sector associated to the mirror A is Ω_{AA} whereas the two-shadow sector associated to mirrors A and B is Ω_{AB}. Correspondingly, we also define the reference images R_{AA} (which are identical to those introduced before), R_{AB}, etc. and the reference angles β_{AA} (also identical to those introduced before), β_{AB}, etc. For the two-shadows sector Ω_{AB}, we set $\beta_{AB} = (\beta_{AA} + \beta_{BB})/2$. We highlight here that the angular intervals introduced before (Γ_A, Γ_B, etc.) always overlap with their neighbors, whereas the sectors (Ω_{AA}, Ω_{AB}, Ω_{BB}, etc.) never overlap (see Fig. 2).

It should be noticed that within a two-shadow sector, each shadow shifts according to Eq. (1), where the reference value β_{AA} depends on the mirror generating that specific shadow. For example, we analyze the two-shadow sector Ω_{AB} between the mirrors A and B, associated to the reference value β_{AB}. The corresponding shifts of each shadow are:

$$shift_A = d \cdot tan\left(\beta - \beta_{AA}\right) \tag{4}$$

$$shift_B = d \cdot tan\left(\beta - \beta_{BB}\right) \tag{5}$$

where $shift_A$ and $shift_B$ are referred to the reference images R_{AA} and R_{BB}, these equations imply that shadows A and B shift differently, and two-shadow images cannot be obtained by merely shifting R_{AB}. So, in principle, the method explained for the single-shadow sectors, does not work for the two-shadow sectors.

However, using the Taylor expansion of Eqs. (4) and (5) around the reference angle β_{AB} of Ω_{AB}, it can be demonstrated that, in a first approximation, the previous method also applies to the two-shadow sectors. Eqs. (4) and (5) can thus be expanded as follow:

$$shift_A = d \cdot \left(tan\left(\beta_{AB} - \beta_{AA}\right) + \frac{\left(\beta - \beta_{AB}\right)}{cos^2\left(\beta_{AB} - \beta_{AA}\right)} + \frac{tan\left(\beta_{AB} - \beta_{AA}\right) \cdot \left(\beta - \beta_{AB}\right)^2}{cos^2\left(\beta_{AB} - \beta_{AA}\right)} + \cdots \right) \tag{6}$$

$$shift_B = d \cdot \left(tan\left(\beta_{AB} - \beta_{BB}\right) + \frac{\left(\beta - \beta_{AB}\right)}{cos^2\left(\beta_{AB} - \beta_{BB}\right)} + \frac{tan\left(\beta_{AB} - \beta_{BB}\right) \cdot \left(\beta - \beta_{AB}\right)^2}{cos^2\left(\beta_{AB} - \beta_{BB}\right)} + \cdots \right) \tag{7}$$

The first terms on the right side of Eqs. (6) and (7) define the positions of the shadows A and B when $\beta = \beta_{AB}$. This can be better understood by comparison with Eq. (1). In other words, they define the shape of the reference image R_{AB}. The second and the following terms are the most important ones as they quantify the shifts of shadows A and B from their positions in R_{AB}. However, from the definition of β_{AB}, we can write:

$$\left(\beta_{AB} - \beta_{AA}\right) = -\left(\beta_{AB} - \beta_{BB}\right) \tag{8}$$

Using this relationship, it is easy to demonstrate that the second term on the right of Eqs. (6) and (7) are equal. Therefore, if $|\beta - \beta_{AB}|$

is small, the following input-output relation can be used for the two-shadow sectors:

$$shift_{AB} \approx \frac{d}{cos^2\left(\beta_{AB}-\beta_{AA}\right)} \cdot \left(\beta-\beta_{AB}\right) \quad (9)$$

This equation applies to the full shadow image, whereas Eqs. (4) and (5) are specific for the shadows *A* and *B*. We also notice the similarity with the linear approximation of Eq. (1). However, the sensitivity is slightly bigger in this case. Indeed, the angle β_{AB}-β_{AA} depends only on the number of mirrors; with eight mirrors, $|\beta_{AB}$-$\beta_{AA}|$ = 22.5 degrees and the ratio between the sensitivities is:

$$\frac{Sensitivity_{AB}}{Sensitivity_{AA}} = \frac{d}{\cos^2\left(\beta_{AB}-\beta_{AA}\right)} \cdot \frac{1}{d} = \frac{1}{\cos^2(22.5degrees)} = 1.17. \quad (10)$$

This means that the sensitivity changes slightly from one sector to the other, which is not ideal. Indeed, a ratio closer to one would be preferable. This can be achieved using a larger number of mirrors as $|\beta_{AB}$-$\beta_{AA}|$ would be smaller; for example, using 10 mirrors would lead to a ratio of 1.10. But, on the other hand, this would also increase the complexity of the system and might not always be viable.

Overall, we have demonstrated that the input-output relation of ASTRAS360 is approximately linear only within the specific sectors and when $|\beta$-$\beta_{AA}|$(or$|\beta$-$\beta_{AB}|$) is small. When the latter is large, and we consider the transition between sectors, the linearity error is not negligible. To reduce it, we propose three methods that can be used at the same time: calibrate each sector separately, use polynomial best-fitting curves to approximate the experimental calibration measurements, and increase the number of mirrors. The first two methods can always be applied and will, therefore, be discussed in the following sections. Increasing the number of mirrors has important technical implications. For example, it might become challenging to find enough color filters that will still allow differentiating the sectors (see Section 3); furthermore, the mechanical design becomes very complex. For these reasons, we did not consider more than eight mirrors for our characterization prototype.

3. Image processing

3.1. Sector identification and measurement refinement

The image processing algorithm presented herein focuses on the main steps required to compute the critical information from the shadow images, namely the variables β_{AA} and $shift_{AA}$ of Eq. (2). These are obtained by first identifying the sector (coarse measurement) followed by fine measuring the *shift* using the correlation between the input image and the reference image, as described in [3].

The main steps of the coarse measurement are depicted in Fig. 4. The image and the plots on the left-hand side of the image refer to single-shadow images and those on the right-hand side correspond to two-shadow images. The processing of both types of shadow images, which differ only slightly from one another, will be described in the following. The shadow images shown in Fig. 4 are representatives of all the images that the proposed sensor encounters. The only expected variables are the horizontal shift of the shadow(s), and the change of the hue (see Video 1). Furthermore, the mechanical specifications of the system were defined such that the shadows are not shifting out of the field-or-view of the image sensor.

Assuming that R_{jk}, G_{jk}, and, B_{jk} are the Red, Green, and Blue values of each pixel and the indexes $j \in [1;J]$ and $k \in [1;K]$ identify the row and the column of the image, we first calculate intensity vector I_k (or simply I) as follow:

$$I_k = 100 \times \frac{\sum_{j=1}^{J}\left(R_{jk}+G_{jk}+B_{jk}\right)}{\max_{k'}\left(\sum_{j=1}^{J}\left(R_{jk'}+G_{jk'}+B_{jk'}\right)\right)} = 100 \times \frac{\sum_{j=1}^{J}\left(Grey_{jk}\right)}{\max_{k'}\left(\sum_{j=1}^{J}\left(Grey_{jk'}\right)\right)} \quad (11)$$

in which $Grey_{jk}$ is the grey level of the pixel *j*, *k*. In Fig. 4, these are shown in the two plots underneath the corresponding shadow images (continuous black line). Then, we count the number n_a of elements of I whose values are bigger than a threshold t_r; these elements are depicted with blue dots in Fig. 4. The number n_a changes consistently from single to two-shadow images; this is visible comparing the number of blue dots in the two intensity plots in Fig. 4. Therefore, when n_a is smaller than a predefined threshold T_v, the shadow image is identified as a single-shadow image, otherwise, it is recognized as a two-shadow image.

In case of a single-shadow image, the index of the mirror contributing to the shadow is identified by analyzing the hue, i.e. color, histogram of the image pixels. The value of the hue is obtained by converting the color representation from RGB (as recorded by the image sensor) to HSV (Hue, Saturation, Value), where we use only the Hue. It should be noticed that pixels with a low grey level (those that are dark in the shadow image) might have a random value of hue because of the electronic noise of the image sensor. For this reason, we plot the histogram of the Hue weighted by the grey level of the pixels as expressed by the following equation:

$$G_{counts}(H) = \sum_{\left\{j,k|H_{jk}=H\right\}} Grey_{jk} \quad (12)$$

where H_{jk} is the Hue of the pixels *j*,*k*. In this way, pixels with higher intensity will count more and the others will produce a negligible effect on the histogram. An example histogram for a single-shadow image is shown in Fig. 4 (bottom-left side) and, as expected, features a single sharp peak. The coordinate of this peak is called $h_{char,}$ and it is very informative. As we will see in Section 3.2, the color filters are chosen such that h_{char} uniquely identifies the single-shadow sector providing a coarse measurement (β_{AA}).

For the two-shadow images, the hue-histogram might be more complicated, showing multiple not well-defined peaks. For this reason, we use only the portions of the two-shadow image as identified by the red (L) and blue (R) rectangles in Fig. 4 (top-right side). These are easy to localize automatically as they correspond to the first and the last elements of I above the threshold t_r. In this way, the expected histograms of the hue of two-shadow images to show two peaks at position h^L_{char} and h^R_{char} as shown in Fig. 4 (bottom-right side). As before, the specific combination of their two coordinates uniquely identifies the two-shadow sectors providing the coarse measurement. We could use the same method also for single-shadow images, but the determination of h_{char} would be less accurate, leading to unwanted difficulties. Some single-shadow images show a different hue on the left and the right sides; for this reason, we decided to use two different methods, as explained above.

The *shift* is measured in the same way for single-shadow sectors and two-shadow sectors. This is done by calculating the correlation between the input shadow image and the reference shadow image of the identified sector. The *shift* is defined by the position of the highest peak of the correlation result.

Finally, as discussed in Section 2, ASTRAS360 shows a non-linear behavior, and a polynomial relationship could be used for describing the input-output relationship for each sector. Therefore, once

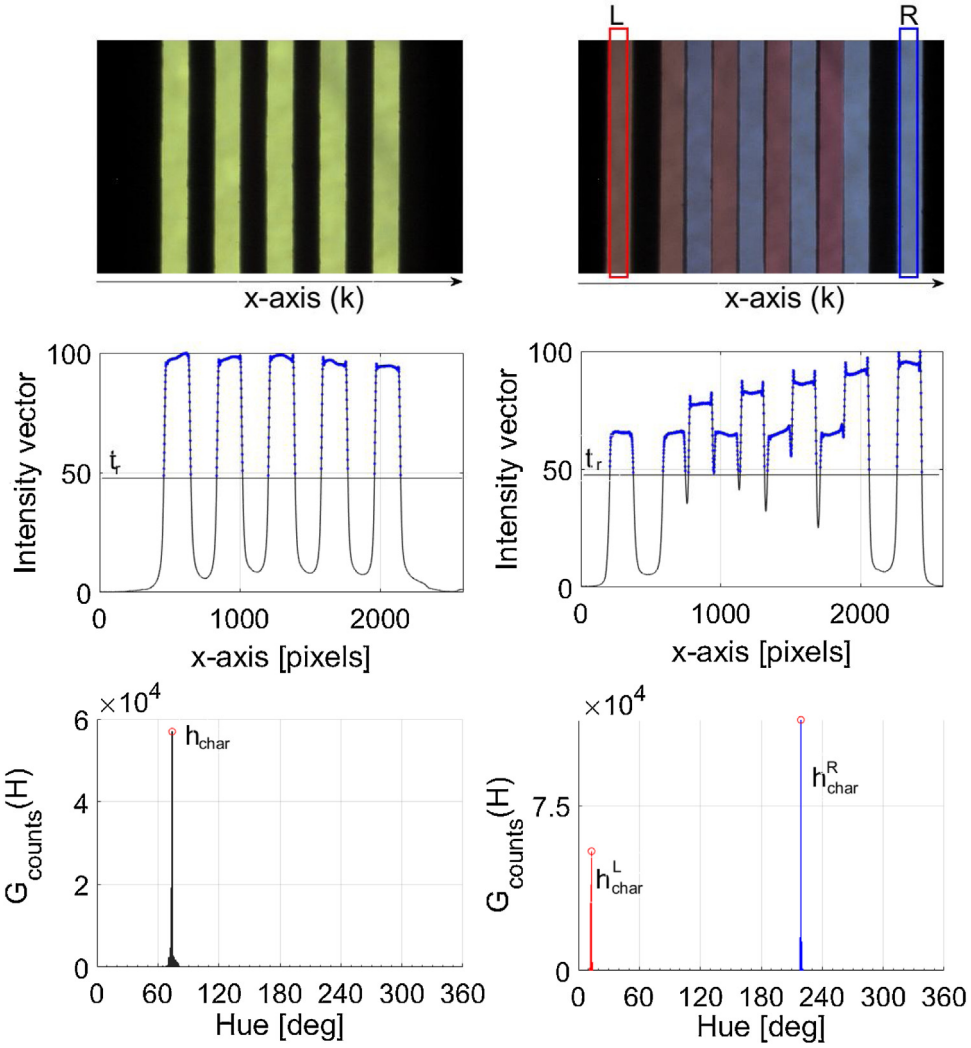

Fig. 4. Image processing for the single-shadow image (left side) and two-shadow image (right side). The two plots in the middle represent the intensity vectors I (continuous black lines). The number of elements above the threshold t_r (indicated with blue dots) is n_a and it is used to distinguish the single-shadow images from the two-shadow ones. The last two graphs are the weighted histograms of the hue; the position of the peaks identifies the sector. (For interpretation of the references to color in this figure legend, the reader is referred to the web version of this article).

the sector is identified (we refer to it as Sector *XX*), instead of Eq. (2) where we use:

$$\beta = \sum_{i=0}^{N} P_{i,XX} \cdot shift^i + \beta_{XX} \tag{13}$$

with β_{XX} (similarly to β_{AA}) as the reference angle of Sector *XX*, $P_{i,XX}$ are the coefficients of the polynomial that best fits the calibration data of that sector, and *shift* is measured in number of pixels.

3.2. Calibration phase

The calibration phase consists of collecting a set of calibration images and simultaneously measuring the corresponding angles β using a calibration standard (e.g., the scale of a rotary mount, see Section 4).

The first step consists of identifying the best value for t_r (see Paragraph 3.1 and the plots of the Intensity in Fig. 4). To do so, we use Otsu's method [38] over the histogram of the values of vectors I of all the calibration images together (Fig. 5). In our experiment t_r was 48.5.

To define the threshold T_v (see Paragraph 3.1), a histogram of the values of n_a can be computed. The histogram we obtained in our experiment is shown in Fig. 6; in this example we can distinguish

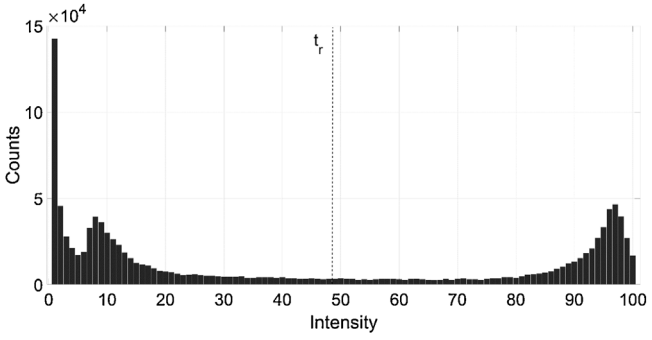

Fig. 5. Histogram of the values of all the intensity values of all the calibration images. The threshold $t_r = 48.5$ was calculated with the Otsu's method.

two main clusters, one around 1750 for the two-shadow images, and one around 910 for the single-shadow images. T_v can be set using Otsu's method; e.g., in our experiment, it was 1184.

Once t_r and T_v are defined, we can label each calibration image as either a single-shadow or two-shadows image. As we also know the corresponding values of β, we can easily identify the border angles between the single-shadow sectors and the adjacent two-

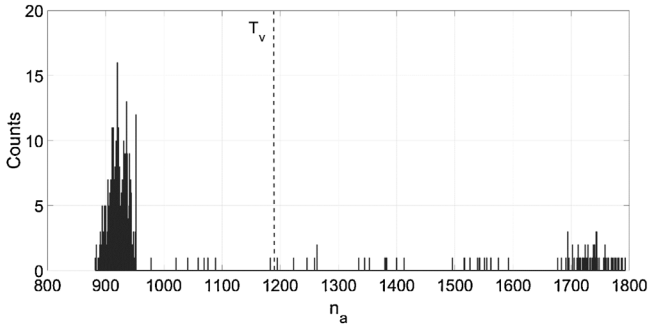

Fig. 6. Histogram of the values of n_a of all calibration images. The threshold $T_v = 1184$ was calculated with the Otsu's method.

shadow sectors (see vertical lines in Fig. 7). In this way, all sectors can be defined, and their reference angles (β_{AA}, β_{AB}, etc.) have to be selected close to their central values. In particular, we selected the reference angles among those acquired during the calibration phase so that we also had the reference images (R_{AA}, R_{AB}, etc.). Fig. 3 shows examples of reference shadow images for single-shadow sectors (R_{AA} for sector AA and R_{BB} and for sector BB) and for two-shadow sectors (R_{AB} for sector AB).

At this point, the characteristic values of the hue (h_{char}, h^R_{char}, h^L_{char}) of all the calibration images can be found and plotted, as shown in Fig. 7. The single-shadow sectors, such as Ω_{AA}, Ω_{BB}, Ω_{CC}, etc., feature only one point (black asterisks) per each value of β and the two-shadow sectors, such as Ω_{AB}, Ω_{BC}, Ω_{CD}, etc., feature two points (blue and red asterisks). From this calibration chart, the rules to associate an input image to its own sector can be set using the corresponding max and min values of h_{char}, h^R_{char} and h^L_{char}. Tables 1 and 2 are the rules related to the calibration chart in Fig. 7.

Finally, the coefficients $P_{i,XX}$ of Eq. (13) are calculated from the calibration data. This is done for each sector following the same procedure as in [3], which consists in finding the best fitting (least square best fit) polynomial for the calibration data.

4. Experimental prototype

The technical drawing of the prototype, photo, and videos of the setup are shown in Figs. 8 and 9, Video 1, and Video 2. This prototype was custom designed, and the majority of its components were 3D-printed with a Fortus 250mc by Stratasys using an ABSplus-P430 thermoplastic.

The main structure of the rotor was the ASTRAS360-dome that hosted 8 mirrors forming an octagon (diameter of the inscribed circle is 50 mm). The mirrors were inserted together with the filters inside 8 narrow pockets of the ASTRAS360-dome in a way that they neatly fit. For the prototype, we used the following filter colors: apple green, salmon, pale blue, pale green, neon blue, deep yellow, peacock, and medium purple. However, this choice was critical as if the colors were not well separated in the hue scale, it would be impossible to distinguish the sectors correctly. Finally, the ASTRAS360-dome could be opened for inspection, but during the calibration and the measurements, it was always closed to avoid external light to be detected by the image sensor. The rotor was screwed on a rotary mount (OptoSigma KSW-656-M6) as a mechanical constraint. The latter also provided a calibration standard thanks to its scale with a 600 arcsec resolution, and we assumed an accuracy of half a tick, which corresponds to 300 arcsec.

The elements of the stator (i.e. image sensor or camera, shadow mask, and LED) were mounted on a 3D-printed support that was placed through the center hole of rotation mount. It was designed to slightly tilt the camera in a way that the vertical component of the light rays intersected the sensor orthogonally. This was important to have a uniform value of the hue over the vertical direction.

The image sensor (Ximea MU9PC, pixel size $2.2 \times 2.2\ \mu m^2$ [37]) was set to acquire RGB images (RGB Bayer mosaic) with an overall resolution of 2592×1944 pixels and 12 bits per pixel. The output, obtained by interpolation, consisted of three channels (RGB) with a resolution of 2592×1944 pixels and 12 bits per pixel. It was essential to disable the automatic *white balance* of the image sensor and set the gain of the RGB channels to one. Indeed, the white balance would try to compensate for the color temperature of the light source by changing the gains of the RGB channels accordingly; this would make the measurement of the hue not repeatable and not comparable as it depends on the proportion between the RGB values.

The shadow mask had five slits (0.4 mm width and 0.8 mm pitch) and was fixed to the image sensor as described in [3] at a distance d of ~1.1 mm. Finally, the LED (Picoled SML-P12) was mounted on a small PCB and secured in a pocket of the support under the camera. This pocket was designed to form two non-transparent screens (beam screens in Fig. 10) next to the LED, which was essential to create the shadow images as described in Section 3. In particular, these beam screens prevented that more than two shadows were cast onto the image sensor. In fact, by limiting the angle of the

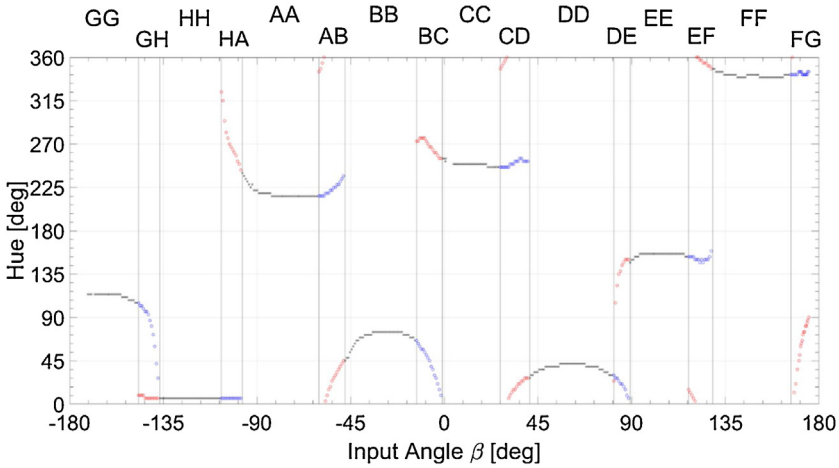

Fig. 7. Example of calibration chart obtained with $t_r = 48.5$ and $T_V = 1184$. The points associated to the single-shadow sectors (h_{char}) are in black; those associated to the left side of a two-shadow sectors (h^L_{char}) are in blue; and those associated to the right (h^R_{char}) are in red. The vertical lines identify the values of β that separate the sectors. (For interpretation of the references to color in this figure legend, the reader is referred to the web version of this article).

Table 1
Rules to associate the hue of the single-shadow images (h_{char}) to the corresponding sector.

Sector Ω	GG	HH	AA	BB	CC	DD	EE	FF
Range h_{char}	[104:106]	[4:8]	[214:242]	[44:76]	[244:256]	[26:43]	[146:158]	[338:350]

Table 2
Rules to associate the hue of the two-shadow images (h^L_{char} and h^R_{char}) to the corresponding sector.

Sector Ω	GH	HA	AB	BC	CD	DE	EF	FG
Range h^R_{char}	[4:10]	[243:326]	[344:360]–[0:46]	[254:278]	[346:360]–[0:28]	[22:152]	[346:360]–[0:16]	[358:360]–[0:92]
Range h^L_{char}	[26:106]	[4:7]	[214:238]	[8:68]	[245:256]	[5:32]	[146:160]	[340:346]

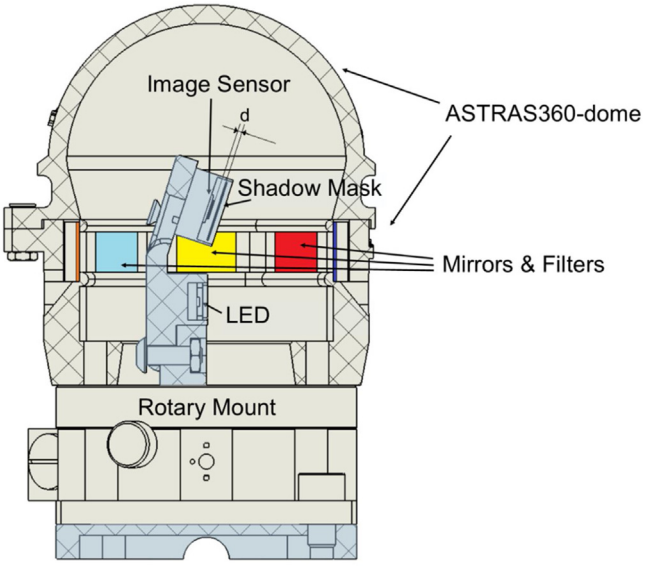

Fig. 8. Section view of the prototype of ASTRAS360. The stator, highlighted in blue, passes through the hole of the rotary mount. (For interpretation of the references to color in this figure legend, the reader is referred to the web version of this article).

Fig. 9. Photo of the characterization prototype featuring a rotary mount. During the tests, the dome was closed in order to prevent the external light to reach the image sensor. The parts were black painted to avoid unwanted light reflections.

light beam, the mirrors were only illuminated when necessary. As a beneficial consequence, the maximum angle of incidence of the light on the camera was also limited, preventing an unwanted drift of the hue (see Sub-section 5.1). Similar beneficial effects could be obtained using a collimating lens in front of the LED. However, non-transparent screens are easier to realize and deploy in a miniaturized version of ASTRAS360.

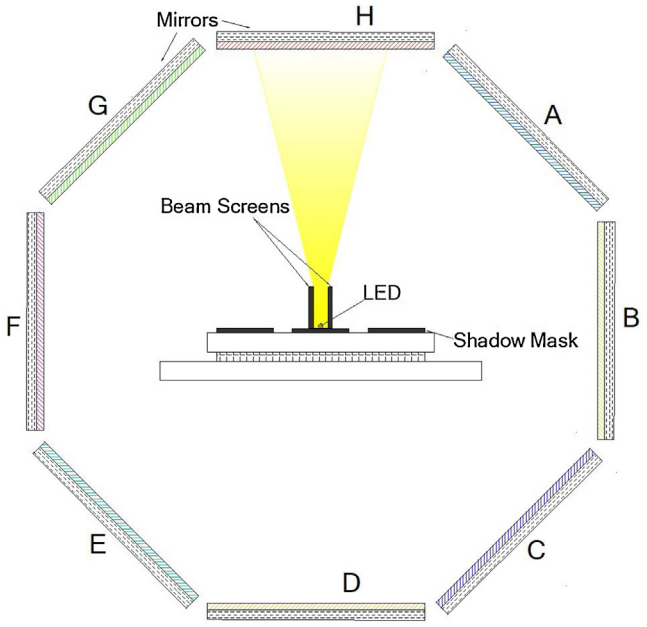

Fig. 10. Beam screens next to the LED limit the light beam so that no more than two mirrors can contribute to shape the shadow image.

5. Experiments and discussion

5.1. Image quality

We verified that all the requirements of the image processing algorithm (see Section 3) were met along with the 360 degrees range. This was done in real-time thanks to the acquisition software (XIMEA CamTool) provided by the manufacturer of the camera. Fig. 3 and Video 1 show some representatives of the shadow images captured by the camera for three different sectors.

We observed a drift of the hue when the angle of the incidence of the light onto the camera was bigger than ~15 degrees. This phenomenon was visible within the two-shadow images as the angle of incidence was bigger. This can be seen in Fig. 3 where shadow B appears brown in R_{AB} whereas it should be pale green as in R_{BB}. Most likely, this drift of the hue was due to the different optical path of the light through the color filters. The effect on the data analysis was that the values h^R_{char} and h^L_{char} had a big variability as visible in the calibration chart (Fig. 7). Anyway, if the range of values of h_{char}, h^R_{char} and h^L_{char} are distinguishable (e.g. like those in Tables 1 and 2), it is always possible to uniquely identify the sectors. However, an accurate selection of the color filters was required to guarantee the correct identification of the sector.

5.2. Calibration and sensitivity

To calibrate the system, we collected 444 shadow images with their corresponding angle β measured with the rotary mount as ground-truth. We then processed the images as described in Section 3 and obtained the histogram of the n_a (Fig. 6), the calibration chart (Fig. 7), the corresponding rules to identify the sectors (Tables 1 and 2), the calibration curves per each sector, and the coefficient $P_{i,XX}$ of Eq. (13) using a third-degree polynomial.

We evaluated the sensitivity of each sector from the linear term of Eq. (13). For the two-shadow sectors, the mean sensitivity was 13 ± 1 pixels/degree, while for the single-shadow sectors it was 12.0 ± 0.1 pixels/degree. The associated error was estimated as three times the standard deviations of the corresponding set. As predicted by the simplified model (Section 2), the sensitivities of the two-shadow sectors were bigger, and the ratio of the mean values was R_E=1.10 ± 0.09. We should compare this result with the theoretical value of the proportion which was estimated in Section 2 as R_T=1.17; however, as the two-shadow sectors were not centered between the two corresponding mirrors (i.e. β_{AB} - $\beta_{AA} \neq 22.5$ degrees in Eq. (13)), an uncertainty has to be associated also to R_T. By considering the reference angles chosen for the two-shadow sectors (see the central angles of the sectors identified in Fig. 7), we considered an error of (β_{AB} - β_{AA}) equal to 5 degrees. Consequently, propagating this error in Eq. (13), we estimated that R_T=1.17 ± 0.08. Therefore, considering the error intervals, R_T and R_E were in agreement.

Finally, it is worth noticing that the values of the sensitivity that we obtained are consistent with those of ASTRAS [3]. In the case of ASTRAS, the sensitivity was measured to be 11.2 pixels/degree instead of 12.0 pixels/degree as compared to ASTRAS360. We attribute this slight discrepancy to the fact that the distance H between the mirror and the sensor was slightly larger in ASTRAS360 (~25 mm) as compared to ASTRAS (~21 mm). In fact, it was measured in [3] that the sensitivity increases with H although the theoretical model does not predict it.

5.3. Precision, resolution, and systematic error

The precision of ASTRAS360 is the standard deviation of repeated measurement. The distribution of 1000 samples was a Gaussian, and the standard deviation was 0.6 arcsec. The precision mainly depends on the noise of the image sensor and on the sensitivity (i.e., on d, see Section 2, and on the pixel size, see [3]); these two parameters were the same in the ASTRAS sensor which was confirmed by the comparable precision we observed.

The precision limits the resolution of ASTRAS360 and, therefore, we used the 6σ-resolution, defined in [35], to evaluate it as 3.6 arcsec, corresponding to 19 bits. It should be noticed that this value can be further improved by selecting an image sensor with lower noise and smaller pixels (see [3]), and by increasing the sensitivity, i.e., the distance d between the shadow mask and the image sensor (see Eq. (1) and Fig. 1).

The systematic error is defined as the deviation of the calibration curve from the best fitting (least square) polynomial line. If the polynomial is a straight line, this error is called linearity error. As ASTRAS360 is not linear (see Section 2), we used third degree polynomials to fit the calibration curves of each sector. The systematic error versus the input angle β is plotted in Fig. 11. The standard deviation of the error was about 230 arcsec over 360 degrees. As this estimation seems limited by the accuracy of the rotary mount (300 arcsec) rather than by ASTRAS360, we believe that this result should be interpreted as a proof of the concept rather than a characterization measurement.

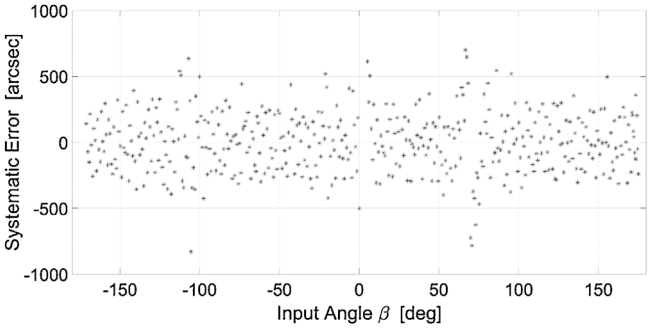

Fig. 11. Systematic error of ASTRAS360 vs the input angle β. The horizontal lines identify the standard deviation of the experimental points.

6. Conclusion

In this work, we discussed the development of a novel absolute rotary encoder concept called ASTRAS360. In particular, we described an approach to extend the measurement range to 360 degrees. We defined a simplified model of the working principle, thanks to which our experimental results were predicted. We developed and presented the processing algorithm, which is a crucial part of the system. To test the working principle and the performance of ASTRAS360, we built a prototype for characterization. The results of these tests were very promising, as the prototype was able to correctly perform the measurements over the full range, with 0.6 arcsec precision, and 3.6 arcsec 6σ-resolution corresponding to 19 bits.

In another work [11], it was demonstrated that ASTRAS360 has the potential to be miniaturized. However, several challenges are still remaining: the proper functioning of the processing algorithm is sensitive to the choice of the color filters and should be improved; a miniaturized version of ASTRAS360, based on a NanEye camera ($1 \times 1 \times 0.5\ mm^3$), has to be built and characterized; a real-time acquisition system has to be implemented in order to acquire and process the images from all the sensors of the medical tracking system [12]; the systematic error should be characterized with a reference encoder with an accuracy better by at least one order of magnitude.

Finally, we believe that the concept of ASTRAS360 can be extended to make it usable also for measuring over two degrees of freedom. This new feature would make ASTRAS360 usable in several other applications such as the measurement of the angles between two consecutive elements of a continuum robot.

CRediT authorship contribution statement

Lorenzo Iafolla: Conceptualization, Methodology, Software, Validation, Investigation, Writing - original draft, Writing - review & editing, Visualization. **Massimiliano Filipozzi:** Methodology, Software, Investigation, Writing - review & editing. **Sara Freund:** Writing - review & editing, Supervision, Project administration. **Azhar Zam:** Writing - review & editing, Supervision. **Georg Rauter:** Conceptualization, Writing - review & editing, Supervision. **Philippe Claude Cattin:** Conceptualization, Methodology, Writing - review & editing, Supervision, Project administration, Funding acquisition.

Appendix A. Supplementary data

Supplementary material related to this article can be found, in the online version, at doi:https://doi.org/10.1016/j.sna.2020.112100.

Declaration of Competing Interest

The authors declare that they have no known competing financial interests or personal relationships that could have appeared to influence the work reported in this paper.

References

[1] W. Birkfellner, J. Hummel, E. Wilson, K. Cleary, Tracking devices, in: Image-Guided Interventions, Technology and Applications, Springer Science, 2008, ISBN: 978-0-387-73856-73857.
[2] P. Gomes, Localization and tracking technologies for medical robotics, in: Medical Robotics, Minimally Invasive Surgery, Elsevier, 2012, ISBN: 978-0-85709-130-137.
[3] L. Iafolla, et al., Proof of principle of a novel angular sensor concept for tracking systems, Sensors and Actuators A: Physical, A 280 (2018) 390–398, http://dx.doi.org/10.1016/j.sna.2018.08.012, Elsevier.
[4] Douglas B. Leviton, Apparatus and method for a light direction sensor, United States Patents, 2009. Patent US 7,924,415 B2.
[5] P. Masa, E. Edoardo, D. Hasler, E. Grenet, Measurement system of a light source in space, World International Patent Organization, 2012. Patent WO 2012/007561.
[6] P. Masa, E. Franzi, C. Urban, Nanometric resolution absolute position encoders, 13th European Space Mechanisms & Tribology Symposium (2009).
[7] D. Hasler, Positioning system and method, European Patent Application, 2016. Patent EP 3 045 932 A1.
[8] E. Grenet, et al., SpaceCoder: a Nanometric 3D Position Sensing Device, CSEM Scientific and Technical Report, 2011.
[9] P. Masa, Measurement system for optical touch trigger or scanning probe with a concave mirror, European Patent Application, 2013. Patent EP 2 615 425 A1.
[10] A. Chebira, et al., HearRestore: Nanotracking for Image-guided Microsurgery, CSEM Scientific and Technical Report, 2015.
[11] L. Iafolla, et al., Preliminary Tests of the Miniaturization of a Novel Concept of Angular Sensors, 2019 IEEE SENSORS, Montreal, QC, Canada, 2019, http://dx.doi.org/10.1109/SENSORS43011.2019.8956732.
[12] L. Iafolla, et al., Data Acquisition System for a Medical Tracking Device Based on a Novel Angular Sensor, 2019 IEEE SENSORS, Montreal, QC, Canada, 2019, http://dx.doi.org/10.1109/SEN-SORS43011.2019.8956777.
[13] W. Kester, Linear and rotary position and motion sensor, in: Sensor Technology Handbook, Elsevier, 2005, ISBN: 0-7506-7729-5.
[14] E.O. Doebelin, D.N. Manik, Doebelin's measurement systems, 6e, in: Doebelin's Measurement Systems, 6e, Mc Graw Hill, 2011, ISBN: 978-0-07-069968-7.
[15] Rotary Encoder Hengstler Website, 2017 www.hengstler.de.
[16] Rotary Encoder RLS Website, 2017 www.rls.si.
[17] M. Howard, A Dummy's Guide to Position Sensors, 2019 https://www.zettlex.com/articles/.
[18] Rotary Encoder Heidenhain Website, 2020 www.heidenhain.com.
[19] AMS, AS5047U - High Resolution Rotary Position Sensor, 2019 https://ams.com/as5047u/.
[20] Renishaw, The Accuracy of Angle Encoders, 2019 https://www.renishaw.com/en/optical-encoders-white-papers–10133.
[21] Renishaw, Data Sheet: RESM Rotary Scale, 2019 https://www.renishaw.com/en/tonic-incremental-encoder-system-with-resm20-rotary-angle-ring–10243.
[22] M. Pisani, M. Astrua, The new INRIM rotating encoder angle comparator (REAC), Meas. Sci. Technol. 28 (4) (2017), http://dx.doi.org/10.1088/1361-6501/aa5af6.
[23] R. Probst, et al., The new PTB angle comparator, Meas. Sci. Technol. 9 (7) (1998), http://dx.doi.org/10.1088/0957-0233/9/7/009.
[24] T. Watanabe, H. Fujimoto, T. Masuda, Self-calibratable rotary encoder, J. Phys. Conf. Ser. 13 (2005) 056, http://dx.doi.org/10.1088/1742-6596/13/1/056.
[25] W. Qiu-Hua, et al., A novel miniature absolute metal rotary encoder based on single-track periodic gray code, 2012, Second International Conference on Instrumentation, Measurement, Computer, Communication and Control, Harbin (2012) 399–402, http://dx.doi.org/10.1109/IMCCC.2012.98.
[26] D.H. Breslow, Installation and maintenance of high resolution optical shaft encoders, Proc. SPIE 0134, Photo- and Electro-Optics in Range Instrumentation (1978), http://dx.doi.org/10.1117/12.956095.
[27] CUI Inc, Absolute, optical Shaft encoder, in: Datasheet of the Series MAS10-256G, 2018, Available online: (accessed on 2020 https://www.cuidevices.com.
[28] J. Seybold, et al., Miniaturized optical encoder with Micro structured encoder disc, Appl. Sci. Basel (Basel) 9 (2019) 452, http://dx.doi.org/10.3390/app9030452.
[29] Faulhaber, Encoders, Optical Encoders, Series PA2-50, 2019 https://www.micromo.com/media/pdfs/PA2-50_MME.pdf.
[30] Farrand Controls, Precision Inductosyn Position Transducer for Industrial, Automation, Aerospace, and Military Applications, 2019 http://www.inductosyn.com/.
[31] Zettlex, Products Datasheet, 2019 https://www.zettlex.com/products/incoder/.
[32] J. Burgner-Kahrs, D.C. Rucker, H. Choset, Continuum robots for medical applications: a survey, Ieee Trans. Robot. 31 (December (6)) (2015) 1261–1280, http://dx.doi.org/10.1109/TRO.2015.2489500.
[33] C. Shi, et al., Shape sensing techniques for continuum robots in minimally invasive surgery: a survey, IEEE Trans. Biomed. Eng. 64 (August (8)) (2017) 1665–1678, http://dx.doi.org/10.1109/TBME.2016.2622361.
[34] AMS NanEye, Miniature CMOS Image Sensors, 2019 https://ams.com/miniature-camera-modules/.
[35] Andrew J. Fleming, A review of nanometer resolution position sensors: operation and performance, Sens. Actuators A Phys. 190 (2013), http://dx.doi.org/10.1016/j.sna.2012.10.016.
[36] MPS Micro Precision Systems AG, Economical Bearing SD 1423XZRY, 2020 www.mpsag.com.
[37] Ximea Image Sensor, 2019 www.ximea.com.
[38] N. Otsu, A threshold selection method from gray-level histograms, IEEE Trans. Syst. Man Cybern. 9 (January (1)) (1979) 62–66, http://dx.doi.org/10.1109/TSMC.1979.4310076.

Biographies

Lorenzo Iafolla received his master degree in physics with honors from the Università di Tor Vergata, Rome (Italy) in 2009. After his studies he worked for several years for two of the most important Italian research institutions (National Institute for Nuclear Physics and National Institute for Geophysics and Volcanology) and for his own enterprise which is specialized in scientific instrumentation (high sensitivity accelerometers). He gained a profound knowledge in precision measurement techniques applied to Particle Physics, Geophysics, Oceanography and others scientific fields. Besides that, he expanded his expertise in designing, assembling, and using mechanical and electronic devices. He has started his Ph.D. in July 2016 in the Planning and Navigation group of the MIRACLE project at the Department of Biomedical Engineering in Allschwil. During his Ph.D., he will develop new minimally invasive tracking techniques using an opto-mechanical position sensor (ASTRAS).

Massimiliano Filipozzi received his B.Sc. degree in Aerospace engineering in 2016 and in 2019 he received the M.Sc. degree Mechatronic engineering from the Politecnico di Torino, Italy. In 2018, he spent six months of his studies at the Universidad Nacional de Cordoba in Argentina. He started to work for his master thesis at the end of 2018 in the Planning and Navigation group of the MIRACLE project at the Department of Biomedical Engineering of the University of Basel. His activity focused on an opto-mechanical position sensor (ASTRAS) for medical tracking systems. Since August 2019, he has started his Ph.D. in the same department continuing the investigation and advancement in the sensor tracking system technology for minimally invasive surgery.

Sara Freund After a B.Sc. in Applied Physics and Engineering delivered by the University of Strasbourg (France) in 2010, Sara Freund received her M.Sc. in Nanoscience from the University of Basel (Switzerland) in 2014. She was awarded the best Master Thesis SNI Prize for her work. For her Ph.D. in the field of experimental solid state physics and surface science, she joined the group of Prof. E. Meyer at the Department of Physics of the University of Basel (Switzerland). During her stay in the group of Prof. Meyer, she studied the anchoring of single dye molecules on the surface of semiconductors by Atomic Force Microscopy under ultra-high vacuum conditions and graduated in 2018 with Summa cum Laude. Since March 2019, she is a postdoctoral researcher in the group of Prof. Ph. Cattin at the Department of Biomedical Engineering of the University of Basel (Switzerland) and co-leads the Planning and Navigation Group of the MIRACLE project, which is dedicated to the development of new minimally invasive navigation systems, as well as innovative visualization of the planning and progress of surgical interventions with the help of virtual and augmented reality techniques.

Azhar Zam received the B.Sc. degree in medical physics from the University of Indonesia, Depok, Indonesia, in 2004, the M.Sc. degree in biomedical engineering from the University of Lübeck, Lübeck, Germany, in 2007, and the Ph.D. degree in advanced optical technologies from the Friedrich–Alexander, University Erlangen–Nuremberg, Erlangen, Germany, with the focus on optical feedback for tissue-specific laser surgery, in 2011. He held several research positions at the University of Waterloo, Waterloo, ON, Canada, the National University of Ireland Galway, Galway, Ireland, and the University of California at Davis, Davis, CA, USA. He joined the Department of Biomedical Engineering, University of Basel, Allschwil, Switzerland, in 2016, as an Assistant Professor in medical laser and optics, where he founded and leads the Biomedical Laser and Optics Group (BLOG). He has authored over 60 peer-reviewed articles, book chapters, books, and patents. His main research interests focus on the development of smart devices for medical therapy, diagnostics and monitoring using novel optical technologies, including smart laser surgery, optical coherence tomography (OCT), photoacoustics, biomedical spectroscopy (e.g. LIBS and Raman), AI-aided optical diagnostics, optical-based wearable sensors, and miniaturized optical systems.

Georg Rauter was born 1980 in Oberndorf bei Salzburg (Austria). He studied mechatronics in mechanical engineering at Graz University of Technology (Austria) and mathematical and mechanical modelling at the engineering school MATMECA, University Bordeaux 1 (France). In 2006, he developed a prototype for diagnosis in spine pathologies at the enterprise AXS Ingenierie (Merignac, France) before joining the SMS-Lab of Prof. Robert Riener (ETH-Zurich, Switzerland). From March 2008 till October 2013, Georg Rauter worked at the SMS Lab as a PhD student in the field

of robot-assisted human motor learning. During his PhD, he developed a robotic rowing trainer that accelerated motor learning by individualized feedback to the human trainee. In 2013, Georg Rauter worked as a postdoc for research in robot-assisted rehabilitation at the Spinal Cord Injury (SCI) Center of Prof. Armin Curt (University Hospital Balgrist, University of Zurich) together with the SMS-Lab (ETH Zurich). During his postdoc Georg Rauter also stayed at University of Southern California (USC), USA with Professors David Z. D'Argenio and Francisco Valero-Cuevas for half a year. At USC, Georg Rauter developed statistical hierarchical models for analysis of a clinical multicenter study with the rehabilitation robot ARMin. Since his PhD, Georg Rauter is a member of the Award Winning Team: 1 st price euRobotics Technology Transfer Award 2014 for the rehabilitation device THE FLOAT, a Multidirectional Transparent Support System for Over Ground Gait Training. In 2015, he became the CTI-project manager for the FLOAT in a joint project between the SCI Center and the company Lutz Medical Engineering (Rüdlingen, Switzerland). As a result, the first medically certified series version of The FLOAT is available on the market since June 2016. In May 2016, Georg Rauter was awarded an Assistant Professorship at the Department of Biomedical Engineering (University of Basel, Switzerland) for the Minimally Invasive Robot Assisted Computerguided LaserosteotomE (MIRACLE) project. Due to the generous funding of this MIRACLE through the Werner von Siemens Foundation (Zug, Switzerland), Georg Rauter could found the Bio-Inspired RObots for MEDicine-Lab (BIROMED-Lab). The main focus of the research in his BIROMED-Lab is: robotic endoscopes for laser ablation of hard tissue, bio-inspired sensor technologies for endoscopic navigation, tele manipulation, automation, kinematics, and control.

Philippe Cattin was born in Switzerland in 1967. He received his B.Sc. degree from the University of Applied Science in Brugg/Windisch in 1991. In 1995 he received the M.Sc. degree*in *computer science and in 2003 the Ph.D. degree in robotics from ETH Zurich, Switzerland. From 2003 to 2007 he was a Postdoctoral Fellow with the Computer Vision Laboratory at ETH Zurich. In 2007 he became an Assistant Professor at the University of Basel and was promoted to Associate Professor in 2015. He is the founder of the Medical Image Analysis Center at the Medical Faculty of the University of Basel. He is currently the head of the recently founded Department of Biomedical Engineering at the University of Basel. His research interests include medical image analysis, image-guided therapy and robotics-guided laser osteotomy. As a Principal Investigator he has finished many projects in these areas and published over 100 papers, patents and book chapter.